Environmental Science & Technology

pubs.acs.org/est

Article

Morphogenesis of Biofilms in Porous Media and Control on Hydrodynamics

Dorothee L. Kurz, Eleonora Secchi,* Roman Stocker, and Joaquin Jimenez-Martinez*

Cite This: *Environ. Sci. Technol.* 2023, 57, 5666−5677

Read Online

ACCESS | Metrics & More | Article Recommendations | Supporting Information

ABSTRACT: The functioning of natural and engineered porous media, like soils and filters, depends in many cases on the interplay between biochemical processes and hydrodynamics. In such complex environments, microorganisms often form surface-attached communities known as biofilms. Biofilms can take the shape of clusters, which alter the distribution of fluid flow velocities within the porous medium, subsequently influencing biofilm growth. Despite numerous experimental and numerical efforts, the control of the biofilm clustering process and the resulting heterogeneity in biofilm permeability is not well understood, limiting our predictive abilities for biofilm-porous medium systems. Here, we use a *quasi*-2D experimental model of a porous medium to characterize biofilm growth dynamics for different pore sizes and flow rates. We present a method to obtain the time-resolved biofilm permeability field from experimental images and use the obtained permeability field to compute the flow field through a numerical model. We observe a biofilm cluster size distribution characterized by a spectrum slope evolving in time between −2 and −1, a fundamental measure that can be used to create spatio-temporal distributions of biofilm clusters for upscaled models. We find a previously undescribed biofilm permeability distribution, which can be used to stochastically generate permeability fields within biofilms. An increase in velocity variance for a decrease in physical heterogeneity shows that the bioclogged porous medium behaves differently than expected from studies on heterogeneity in abiotic porous media.

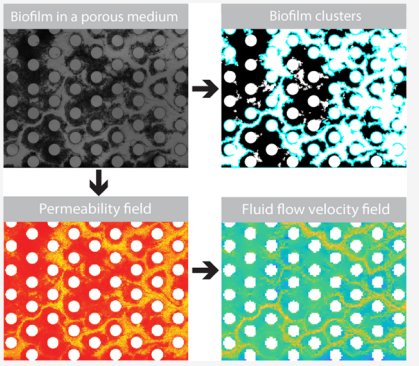

KEYWORDS: *porous media, biofilm cluster dynamics, permeability heterogeneity, fluid flow velocities*

1. INTRODUCTION

Biofilms, the sessile bacterial lifestyle in which cell aggregates embed themselves in a self-secreted extra-cellular polymeric matrix, are frequently found in porous environments.[1] By growing in the pore space, biofilms lead to bioclogging of the porous medium and alter the local flow.[2−5] The presence of other immiscible phases, such as air, has a similar impact,[6] yet biofilms have their own dynamics due to the growth of the cells. Alteration of the local flow increases the range of water velocities within the pore space,[6] creating more pronounced high- and low-velocity regions and consequently modifying the distribution of nutrients and chemicals within the biofilm−porous medium system.[7−9] A mechanistic description of the biofilm growth dynamics under diverse hydrodynamic conditions and of the interplay between flow and growth is of interest in bioremediation and filtration, among others, to optimize application design.[10−12]

Biofilms have a complex structure composed of bacterial cells embedded within extra-cellular polymeric substances (EPS) such as polysaccharides, proteins, and extra-cellular DNA.[13] The matrix is frequently crossed by micron-sized channels that enable internal solute transport,[14] and contribute to the permeability and porosity.[2,15−17] Biofilms can be described as clusters with an irregular morphology, which can be quantified by the fractal dimension,[18,19] where a smaller fractal dimension represents a less complex biofilm shape.[20,21] The fractal dimension has been used to measure the degree of raggedness of the biofilm surface, the perimeter of a section, and internal structure.[19,21−24] Besides the fractal dimension, several other approaches based on image analysis have been used to quantify biofilm growth dynamics, including entropy (the randomness of the biofilm image pixel distribution),[21] the diffusion distance (the minimum distance from the cells in the cluster to the open pore space),[24] the total bioclogging degree, as well as the biofilm cluster size and shape from images.[25] The quantification of biofilm development in terms of one or more of these descriptors enables the comparison between different flow rate and pore size conditions, to unravel their influence on the biofilm growth dynamics.

To study the influence of biofilms on hydrodynamics in porous media, both experimental and numerical approaches have been proposed. Experiments to measure the flow field and obtain the velocity distribution have employed particle image

Received: November 25, 2022
Revised: March 6, 2023
Accepted: March 14, 2023
Published: March 28, 2023

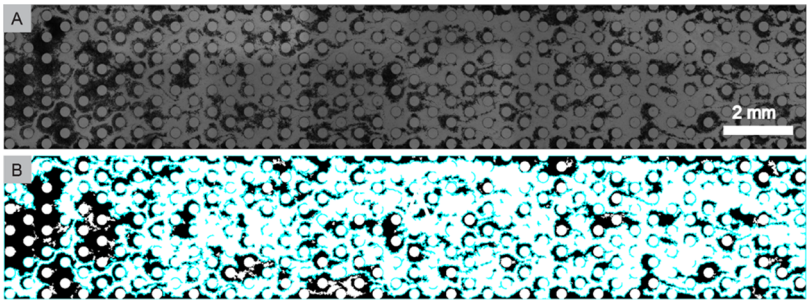

Figure 1. (A) Bright-field image of *B. subtilis* biofilm grown in the microfluidic porous medium with pore size d = 300 μm and flow rate Q = 1 mL/h, taken at t = 10 h. The scale bar applies to both panels. (B) Binarized image of panel A showing the clusters outlined in cyan.

velocimetry and particle tracking velocimetry in both two-dimensional (2D) and three-dimensional (3D) porous media.[3,26] Unfortunately, the micron-sized particles that are often used as tracers can become trapped within the biofilm structure, thus hindering a complete and reliable characterization of the velocity field. An alternative strategy is to use numerical models.[27−31] However, the modeling of biofilms presents challenges related to their structural heterogeneity and complex rheology. In particular, for biofilms grown in flow conditions, parameters such as biofilm permeability and porosity are challenging to measure *in situ* at the spatial resolution needed for accurate modeling.

Current studies have modeled fluid flow velocities within biofilms in porous media from experimental images[28,29] assuming a constant permeability and porosity value for the entire biofilm, for a range of different values of permeability and porosity (typically from 10^{-15} to 10^{-7} m^2 for biofilm permeability and from 0.2 to 0.93 for biofilm porosity).[9,25,28,29,32,33] More recently, a "digital twin" approach has been proposed, in which the biofilm images were converted to a numerical model and the biofilm's biomass at a given location is considered impermeable or permeable based on its optical density.[34] This approach was used to show that biofilms can be considered a permeable medium by comparing simulated and experimental permeability reductions of the porous medium.[34] In another approach, the porosity of the biofilm has been inferred by converting experimental images to local density maps of the biomass. This revealed that the presence of biofilm increases the fluid flow velocity heterogeneity and the spreading of a transported solute.[30] Furthermore, in abiotic porous media, the mosaic of high and low velocities within porous media enhances the reactivity, due to the enhanced creation of concentration gradients.[35,36] Despite these advances, the temporal evolution of the permeability field within porous media during bioclogging, its relation with the aggregation process of biofilm clusters, and its dependency on pore size and flow rate have remained largely unknown.

In this work, we contribute to addressing this gap by combining experiments and numerical modeling to study the interaction between biofilm clustering dynamics and local hydrodynamics. We investigate three combinations of flow rate and pore size. First, we analyze the temporal behavior of biofilm cluster formation from experiments in which we image biofilm formation over space and time. Then, we develop a method to quantify the permeability field from the experimental bright-field microscopy images of the biofilm-porous medium system. Next, we combine the determined permeability field and computational fluid dynamics to obtain the temporal evolution of the velocity field of the biofilm-porous medium system. Finally, we use statistical analysis to establish the time-resolved relationship between the hydrodynamics and the physical heterogeneity in the biofilm-porous medium system, which is directly relevant to chemical transport. These analyses yield insights into the influence of flow rate and pore size on biofilm cluster formation and provide a new method for determining how the biofilm influences the local velocity field in the biofilm-porous medium system.

2. MATERIALS AND METHODS

An overview of the workflow of the methods is shown in SI Figure S1.

2.1. Microfluidic Experiments. We used microfluidic devices to image biofilm development in a porous medium with a defined geometry and controlled hydrodynamic conditions. The porous medium was fabricated as an array of regularly arranged cylindrical pillars located at a distance equal to their diameter, hereafter referred to as pore size (Figure 1). We investigated three experimental conditions by varying the flow rate and the pore size. Our baseline experiment was conducted at a flow rate Q = 1 mL/h with pore size d = 300 μm, resulting in an initial mean fluid flow velocity, $\overline{u}_o$, of 0.96 mm/s and an initial average shear rate, $\dot{\gamma}_0$, of 10 s^{-1}. Further experiments were conducted at Q = 1 mL/h with d = 75 μm ($\overline{u}_o$ = 0.96 mm/s, $\dot{\gamma}_0$ = 38 s^{-1}) and at Q = 0.2 mL/h with d = 300 μm ($\overline{u}_o$ = 0.19 mm/s, $\dot{\gamma}_0$ = 2 s^{-1}). The initial porosity (*i.e.*, the porosity before any biofilm growth in the porous medium) of all of the microfluidic devices was the same and equal to n = 0.77.

2.1.1. Bacterial Cultures. Bacterial cultures of wild-type *Bacillus subtilis* NCIB 3610, a soil-born model organism for biofilm formation, were prepared by inoculating 3 mL of nutrient broth n° 3 (Sigma-Aldrich) (composition: meat extract 1 g/L, peptone 5 g/L, NaCl 5 g/L, yeast extract 2 g/L) from a frozen glycerol stock. The bacterial solution was incubated overnight at 30 °C while shaking at 200 rpm. On the day of the experiment, the solution was diluted 1:1000 in fresh nutrient broth. We then incubated the diluted solution under the same conditions described above until OD_{600} = 0.1 (measured using a cell density meter), to obtain motile cells in early exponential stage.

2.1.2. Microfluidic Fabrication and Assay. Microfluidic devices were fabricated using standard soft lithography techniques with 10% w/w cross-linking agent in polydimethylsiloxane (PDMS) solution (Sylgard 184 Silicone Elastomer Kit, Dow Corning).[37] Devices were washed with 2 mL of the nutrient solution prior to loading of the bacterial solution. The bacterial solution was loaded into the microfluidic device by

https://doi.org/10.1021/acs.est.2c08890
Environ. Sci. Technol. 2023, 57, 5666−5677

drawing it into the microchannel from a centrifuge vial connected to the outlet via tubing. Syringes with the nutrient solution were separated from the microfluidic device by a 1.2 μm sterile filter (Pall Corporation) to prevent bacterial contamination in the nutrient solution during the withdrawal. The bacterial suspension was left in the microfluidic device without flow for 3 h to allow surface attachment of the bacterial cells. Thereafter, we imposed flow of nutrient solution by setting a flow rate (Q = 1 or 0.2 mL/h) using a syringe pump (PHD Ultra, Harvard Apparatus). Imaging of biofilm formation for 24 h at 25 °C was performed on an inverted microscope (Ti Eclipse 2, Nikon) using a digital camera (Orca, Hamamatsu). We performed time-lapse imaging in bright-field configuration (4× objective, NA = 0.13, 1 frame every 6 min). An array of 16 fields of view spanning the porous domain of the microfluidic device was imaged (13,500 × 2500 pixels corresponding to 22 mm × 4 mm). The pressure difference caused by biofilm growth was recorded using a pressure sensor (MPS, Elveflow) placed upstream of the porous domain (SI Figure S1). The pressure reading was set to zero in the software recording the pressure measurements prior to biofilm growth, to measure the pressure difference caused by biofilm growth.

2.2. Cluster Analysis. Stitched bright-field images from the 16 fields of view were aligned using the function "StackReg" in Fiji ImageJ[38] (setting: RigidBody). The images were normalized by dividing each image by the first image of the corresponding time-lapse in order to obtain values between 0 and 1 for the calibration of the image intensity versus the permeability (see next section). Therefore, in the following, the image intensity will be referred to as relative intensity, I_s. Images were binarized with a threshold of I_s = 0.6 to identify the outline of the biofilm, where the value of 0.6 was determined by visual inspection of the performance in determining the outline. From the binarized images, individual bodies were extracted. Bodies smaller than 100 pixels (corresponds to 1062 μm^2) were removed to reduce noise and facilitate cluster analysis. Cluster analysis was then performed to determine the number of clusters in the porous medium (N_c), the mean cluster area ($\bar{A}$), and the fractal dimension of the system (D_f). Cluster analysis was performed in Fiji ImageJ (with the plugins Particle Size Distribution and Fractal Box Counter). Characterization of the cluster size distribution included only clusters before percolation was reached (*i.e.*, before the time at which a single biofilm cluster formed that spanned the entire length of the porous medium from inlet to outlet). The size of each cluster was quantified as the radius of gyration of the cluster, $R_g = \sqrt{A/\pi}$, previously used in cluster analysis of both abiotic and biotic systems.[39,40]

2.3. Permeability Field of the Biofilm-Porous Medium System. This section describes the methodology to convert bright-field microscopy images of the biofilm-porous medium system into a permeability field, with the goal of then determining the fluid flow velocity field in the system through a numerical model accounting for the determined permeability field. First, we obtained the effective permeability of the biofilm (Section 2.3.1) to calibrate a model function derived from an approach used in light transmission micro-tomography (Section 2.3.2). This novel model function allowed us to convert the biofilm-porous medium images to a permeability field and then simulate the fluid flow velocity in the biofilm−porous medium system using a numerical model (Section 2.4).

2.3.1. Effective Permeability of the Biofilm. To obtain the effective permeability of the biofilm, we performed numerical simulations in Comsol Multiphysics 5.5 using models created from the experimental images. The images were segmented to identify the biofilm geometry within the porous medium at five experimental time points (SI Table S1). The segmented images were then used to generate the biofilm models using the "mphimage2geom" function in MatLab (Mathworks) (parametrization "type", "solid", and "mindist", "4") and then imported into COMSOL Multiphysics 5.5, the numerical solver used to solve for the fluid flow. Steady-state velocity fields were solved based on a Darcy−Brinkman formulation.[41] The domain of the porous medium without biofilm was modeled by the incompressible Navier−Stokes formulation

$$\begin{aligned} &\rho(u\cdot\nabla)u = \nabla\cdot[-pI + \mu(\nabla u + (\nabla u)^T)] + F \\ &\rho\,\nabla\cdot u = 0 \end{aligned} \tag{1}$$

where ρ is the liquid density (1000 kg/m^3), u is the fluid velocity, p is the pressure, I is the identity matrix, μ is the dynamic viscosity (0.001 kg/m/s), and $F = u\cdot\frac{\mu}{\kappa_h}$ is an additional term accounting for the effect of the third dimension on the depth-averaged velocity. The latter term includes the drag force exerted on the liquid by the lower and upper boundary walls in the experiments.[42,43] κ_h is the permeability of a channel bounded by two parallel walls separate by a distance h and can be approximated as $\kappa_h = \frac{h^2}{12}$ (in our system, h = 100 μm and $\kappa_h = 8.3 \times 10^{-10}$ m^2).[42]

The Brinkman equation, which accounts for the flow transition from open flow to Darcy flow, is used to solve the flow through the biofilm, where

$$\begin{aligned} \frac{\rho}{n_b}(u\cdot\nabla)u\frac{1}{n_b} = \nabla\cdot\Bigg[-pI + \frac{\mu}{n_b}\Bigg(\nabla u + (\nabla u)^T \\ - \frac{2}{3}\frac{\mu}{n_b}(\nabla\cdot u)I\Bigg)\Bigg] \\ - \left(\frac{\mu}{\kappa_{be}} + \varphi n_b\rho|u| + \frac{Q}{n_b^2}\right)u + F \\ \rho\nabla\cdot u = Q \end{aligned} \tag{2}$$

with Q the flow rate, n_b the porosity of the biofilm matrix, κ_{be} the effective permeability of the biofilm matrix, and φ the parameter in the Ergun equations. The porosity of the biofilm was set to a constant value 0.9[28,44] to determine κ_{be}. Note that $\varphi n_b\,\rho|u|$ is negligible in our case as $Re = \frac{\rho\cdot u\cdot d}{\mu}$ <10, *i.e.*, inertial effects are small at most.

The geometry of the bioclogged porous domain was meshed in Comsol Multiphysics using a triangular method (approximately 1−4 × 10^6 elements). The numerical simulations of eqs 1 and 2 were conducted with a direct, stationary, multifrontal, massively parallel sparse direct solver (MUMPS), with a relative tolerance of 0.001 for the dependent variables, velocity and pressure. As boundary conditions, we imposed a constant inflow velocity at the inlet of the porous domain, obtained from the flow rates used in the experiments, and zero pressure at the outlet of the porous domain. The no-slip condition was imposed at the perimeter of the cylindrical pillars and on the side walls of the domain.

https://doi.org/10.1021/acs.est.2c08890
Environ. Sci. Technol. 2023, 57, 5666−5677

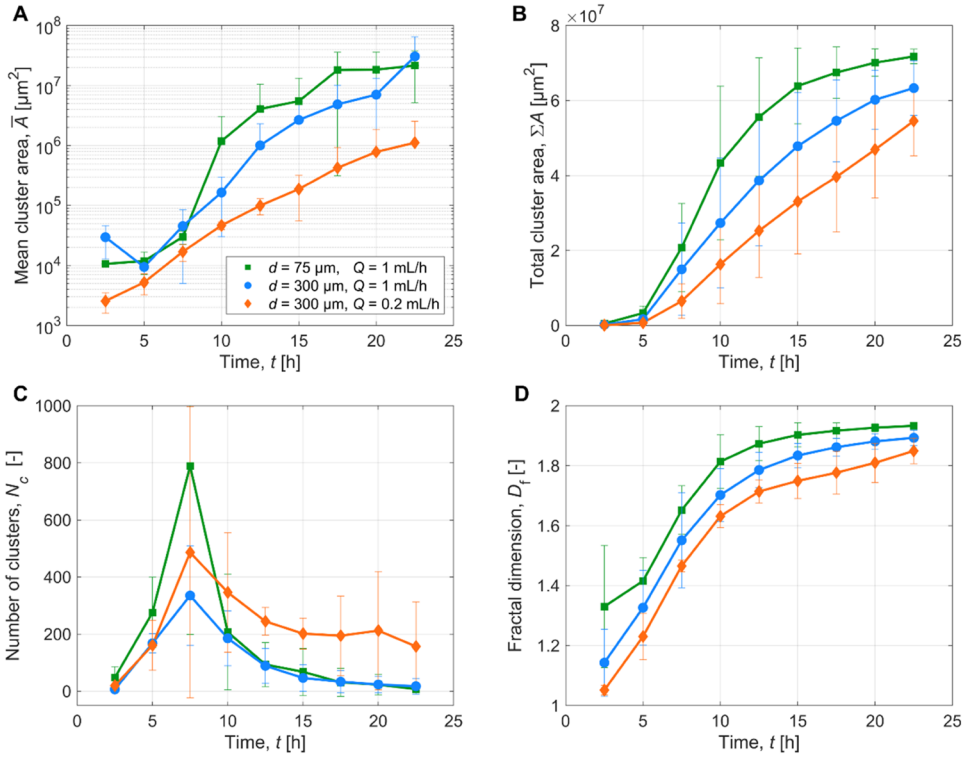

Figure 2. Biofilm cluster dynamics. Temporal evolution of (A) mean cluster area $\bar{A}$, (B) total cluster area $\sum A$, (C) number of clusters N_c, and (D) fractal dimension of the biofilm D_f within the porous medium. Symbols and colors stand for the different experimental conditions of pore size and flow rate (green square, d = 75 μm, Q = 1 mL/h, blue circle, d = 300 μm, Q = 1 mL/h; orange diamond, d = 300 μm, Q = 0.2 mL/h). Bars represent the standard deviation of the mean of experimental triplicates.

The unknown effective permeability of the biofilm, κ_{be}, was obtained by the inverse method, *i.e.*, running simulations for different permeability values of the biofilm and minimizing the difference between the measured and the simulated pressure drop caused by the biofilm (see SI Table S1). The value of κ_{be} is expected to be the geometric mean of the local values of permeability for a two-dimensional, isotropic, multilog Gaussian field.[45,46]

2.3.2. Permeability Field from Light Transmission Micro-Tomography. The Lambert−Beer law relates the transmitted light intensity I_s to the mass per unit volume of the material through which the light is traveling. In our case, I_s is the local normalized intensity, *i.e.*, the intensity of a given pixel in the image, and the Lambert−Beer law reads

$$\ln(I_s) = -\epsilon^* \cdot c \cdot h \tag{3}$$

with ϵ^* an absorption coefficient depending on the substrate, c the local mass per unit volume (*i.e*, at position (x, y)), and h the thickness of the substrate, or here the porous medium microfluidic device. As ϵ^* and h are considered constant, they can be combined into a single parameter $\delta^{-1} = \epsilon^* \cdot h$, eq 3 can then be rewritten as

$$c = -\delta \ln (I_s) \tag{4}$$

With the assumption that c is inversely proportional to the local porosity n (see the SI for details), this yields a relation between the light intensity I_s and the porosity n of the form

$$n = (-\beta \ln(I_s))^{-1} \tag{5}$$

where β includes the parameter δ as well as the proportionality constant between c and n. Equation 5 has a comparable form to relationships established in previous work.[47,48] The porosity n is related to the permeability κ by a power law of the form[49,50]

$$\kappa = \kappa_h \cdot n^{\alpha} \tag{6}$$

with κ_h being the permeability of the microfluidic channel. By combining eqs 5 and 6, we obtain the final model equation linking the permeability κ and the normalized transmitted light intensity I_s

$$\kappa = \kappa_h \cdot (-\beta \ln (I_s) + \gamma)^{-\alpha} \tag{7}$$

where α, β, and γ are parameters defining the shape of the function. The parameter γ has been set as 1 to ensure that $\kappa = \kappa_h$ for the maximum value of the normalized intensity I_s, which corresponds to the case in which there is no biofilm, *i.e.*, the pore space is empty and thus the permeability is $\kappa_h = 8.3 \times 10^{-10}$ m^2 (see Section 2.3.1).

The geometric mean of I_s values within the biofilm for an image (*i.e.*, time step) is expected to correspond to the value of κ_{be}. Using these values as data points for the derived model (five data points corresponding to five time points per experimental condition, SI Table S1), parameters α, β, and γ in eq 7 were fitted for each experimental condition separately by nonlinear least-squares fitting. Three other generic models for permeability as a function of light intensity (linear, exponential, and power law) were also fitted for comparison to data from the baseline experiment (Section 2.1, and SI Table S2). All of the fitted models were then used to convert the relative intensities of the images to permeability fields at single-pixel resolution.

https://doi.org/10.1021/acs.est.2c08890
Environ. Sci. Technol. 2023, 57, 5666−5677

2.4. Numerical Simulation of the Fluid Velocity Field. We numerically simulated 2D, steady-state Darcy flow in the entire pore space for the five time points assessed in the experiments, based on the instantaneous, spatially explicit permeability fields $\kappa(x,y)$ obtained with the procedure laid out in the previous section. We used Darcy's law:

$$u = -\frac{\kappa}{\mu}\nabla p$$
$$\nabla\cdot(\rho u) = Q \quad (8)$$

The geometry was meshed using a triangular method (with 1−4 × 10^6 elements, depending on the time point and biofilm amount within the porous medium). In this case, the dependent variable was the pressure and boundary conditions were set as described earlier (Section 2.3.1).

2.5. Statistical Analysis to Quantify Heterogeneity of the Permeability and the Velocity Field. The multi-Gaussian distribution is the standard log-normal statistical model used to describe a spatially heterogeneous permeability,[51] including cases with extremely high values of permeability connected through channels that can span the entire length of the domain.[52] In order to quantify the heterogeneity of the permeability field, the latter was characterized by log-normal point statistics with variances of the log permeability $\sigma^2_{\ln\kappa}$. The spatial continuity of the resulting permeability field was calculated using the correlation length ζ from a variogram.[51,53] The spatial heterogeneity of the resulting velocity field was characterized by its variance σ^2_u. This was separately done for each time point and for all conditions (flow rates and pore sizes).

3. RESULTS AND DISCUSSION

3.1. Biofilm Cluster Dynamics. *3.1.1. Temporal Dynamics of Cluster Number, Area, and Coverage.* In our experiments, we found that the biofilm forms clusters, which appear as 2D structures in the images (Figure 1A,B). As seen in Figure 1A, the colonization of pillars by the biofilm is also considered a cluster. The growth of clusters at random locations in the porous medium is a consequence of the random initial attachment of bacteria to the solid surfaces. This type of colonization generates heterogeneity in the initially homogeneous porous medium. Therefore, the characterization of the biofilm cluster morphogenesis will provide insight into the temporal evolution of the resulting complexity in the biofilm-porous medium systems.

The mean cluster area ($\overline{A}$) and the total cluster area ($\sum A$) were used to characterize the temporal evolution of biofilm growth within the porous medium under different experimental conditions (Figure 2A,B). Although we found a similar value of $\overline{A}$ for different pore sizes (d) and flow rates (Q) at early time points (0−7.5 h), the mean cluster area $\overline{A}$ remained systematically smaller throughout the experiment for the lower flow rate (Q = 0.2 mL/h) with d = 300 μm, compared to the experiment at the higher flow rate. This indicates that the flow rate, and therefore the initial fluid flow velocity, exerts an important control on the mean cluster area (Figure 2A). In contrast, the total cluster area $\sum A$, which describes the bioclogging process in the entire porous medium, increased more rapidly for the smaller pore size (d = 75 μm) compared to the experiment at a larger pore size at the same flow rate (Figure 2B), despite the initial porosity n being the same. The faster clogging at smaller values of d can be explained by a filtration effect as well as a larger total surface area available for biofilm development, *i.e.*, a larger number of points for bacterial attachment as nucleation sites for biofilm formation. This was confirmed by the temporal evolution of the number of clusters (N_c), where at early time points (0−7.5 h) we observed a larger number of clusters for the smaller value of d (Figure 2C). For all experimental conditions, N_c increased over time until the point at which cluster coalescence counterbalanced the creation of new clusters. Interestingly, this occurred at the same time points for all three experimental conditions. Thereafter, N_c decreased due to cluster coalescence. From these experiments, we conclude that cluster coalescence dynamics are largely independent of d and Q under the conditions studied here, whereas the mean cluster area is most affected by the flow rate and the total cluster area, and hence bioclogging, is controlled by both the pore size and the flow rate.

In summary, we observed the formation of spatially distributed clusters during the growth of *B. subtilis* biofilm within the porous medium. Spatio-temporal patterns during biofilm formation have also been observed in *Escherichia coli* using non-motile and non-chemotactic strains grown in flow in straight (*i.e.*, non-porous-media-like) millifluidic channels.[54] The emergence of cluster patterns has been suggested to result from the interplay of cell−cell and cell−surface interactions.[54] A mechanism of phase separation based on a density-regulated decrease of bacterial motility, together with logistic growth, has also been proposed to result in cluster patterns.[55] While the temporal evolution of cluster number and coverage has been studied on flat surfaces,[56] the cluster dynamics for biofilms we report here emerge robustly under conditions realistic for porous medium environments, namely, biofilms growing under confinement and continuous nutrient flow. The fact that a higher flow rate promotes larger clusters could be explained by a higher nutrient mass flux. The clogging of the entire porous medium occurring faster for the smaller pore sizes at the higher flow rate may be a result of the filtration effect or the higher number of nucleation sites for clusters. Furthermore, growth under higher shear stress is known to create more compact and coalescent biofilms,[57] which could also contribute to faster bioclogging as shear rates are higher in the smaller pores for the same Q. Further studies have found that the accumulating mechanical stresses that accompany growth can determine the morphogenesis of clusters, including their internal reorganization or damage as pieces are broken away, and their coalescence.[58,59] The interplay between the biofilm cluster growth and the shear stresses is accompanied by the formation of preferential flow paths at later time points.[60] Concluding from our results, the fluid flow, which includes the transported nutrients and the physical forces generated by it, and the geometry of the environment shape the biofilm cluster dynamics by influencing, *e.g.*, the mean cluster area as well as the cluster number.

3.1.2. Fractal Dimension of Biofilm Clusters. Experiments revealed that dispersed individual clusters aggregate and grow into larger clusters with fractal-like morphology (Figure 1A). The fractal dimension (D_f) increased from a range of 1.05−1.33 to a range of 1.84−1.93 from t = 2.5 to 22.5 h, for all experimental conditions (Figure 2D). The increase in D_f with time means that the overall morphology of the cluster becomes more rough and is consistent with studies of biofilms grown in open channels.[25] Additionally, the values of D_f we measured are in accordance with the values previously determined for

https://doi.org/10.1021/acs.est.2c08890
Environ. Sci. Technol. 2023, 57, 5666−5677

biofilms in porous media (*e.g.*, $D_f \sim 1.13-1.54$[21]). Although a maximum value of $D_f \sim 1.74$ (thus lower than the values we measured late in our experiments) would be expected from gelation models and other cell systems in the absence of solid obstacles and for an infinite domain,[40,61] our observed final range of values $D_f \sim 1.84-1.93$ is in accordance with the value of $D_f = 1.89$ observed for percolating water clusters in 2D porous media.[62] This accordance hints at a similarity in the behavior of abiotic (*e.g.*, air) and biotic (*e.g.*, biofilm) clusters in porous media.

The temporal evolution of the fractal dimension revealed that a smaller pore size (d) at the same flow rate (Q) is associated with a larger value of D_f. This may be explained by using findings from colloid science, where an increase in concentration and the occurrence of coalescence have been used to explain an increase in D_f.[63] Analogously, a more fractal-like morphology under these conditions could be caused by the more frequent coalescence of biofilm clusters, due to the larger number of clusters (N_c) and a greater mean area ($\overline{A}$) (Figure 2A,C).

The fractal dimension of biofilm clusters is a powerful parameter governing not only geometrical properties but also hydrodynamics within the biofilm-porous medium system.[64] The fractal dimension quantifies the roughness of the biofilm-fluid flow interface and could thereby be considered a proxy for the modified drag force of the fluid when in contact with the biofilm. Thereby, the fractal dimension of the biofilm captures the effect of cluster morphology on the fluid flow between clusters. Especially for experiments with the smaller value of d, the systematically larger D_f observed in our experiments could be linked with a higher drag force as found for flow past fractal aggregates,[65] which demonstrates how the biofilm cluster morphogenesis influences the local hydrodynamics.

3.1.3. Characteristics of the Biofilm Cluster Size Distribution. The characterization of the cluster size distribution within the porous medium was done using the radius of gyration (R_g), which corresponds to the radius of a circle of equivalent area to the one of a biofilm cluster.[39] This revealed that the probability density function $p(R_g)$ follows a scaling $p(R_g) \propto R_g^{\tau}$, with τ evolving in time between -2 and -1 for most replicates of all experimental conditions studied (Figure 3) (see also SI Figure S2 for the replicates and SI Figure S3 for the temporal evolution of τ). τ initially ($t = 5$ h) decreases to values in the order of -2 (or smaller) and thereafter increases and stabilizes to a mean value of $\tau = -1.27$ for $Q = 1$ mL/h and $d = 300$ μm, $\tau = -1.46$ for $Q = 1$ mL/h and $d = 75$ μm and $\tau = -1.64$ for $Q = 0.2$ mL/h and $d = 300$ μm (SI Figure S3). The time point at which τ reaches the value of -2 corresponds to the time point before the cluster coalescence counterbalances cluster creation ($t = 7.5$ h), an important time point in the biofilm cluster morphogenesis (Figure 2C). As in percolation theory,[66] these scaling values for the cluster size distribution of the biofilm within the porous medium can be used to generate spatio-temporal biofilm distributions in numerical simulations and upscaled models. A similar scaling has been observed in multiphase systems, where immiscible phases coexist, both under confined and unconfined conditions. For those systems, τ was -2 for the nonwetting phase clusters in unsaturated porous media, and without the displacement of the nonwetting immiscible phase.[39,67] The same scaling of -2 was found for bubble size distributions in the ocean.[68] A value of $\tau = -1.90$, thus slightly larger than -2, has also been observed under dynamic steady-state multiphase

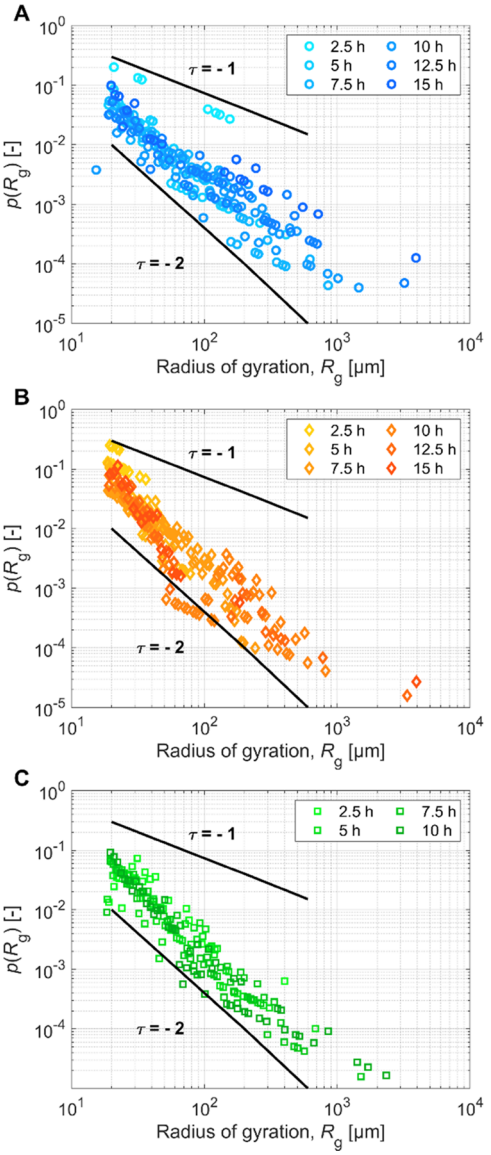

Figure 3. Probability density function of the radius of gyration R_g of biofilm clusters at different time points (color-coded as denoted in the legend) for (A) $d = 300$ μm and $Q = 1$ mL/h (circles), (B) $d = 300$ μm and $Q = 0.2$ mL/h (diamonds), and (C) $d = 75$ μm and $Q = 1$ mL/h (squares). The scaling $p(R_g) \propto R_g^{\tau}$ was found to yield a best-fit exponent between $\tau \sim -2$ and -1 (see SI Figure S3).

flow conditions in porous media, which is a system that closely resembles ours.[69] The similarity between our biofilm-porous medium system and certain abiotic systems (*e.g.*, air or oil within a water-filled porous medium) suggests that the cluster size distribution is strongly influenced by the porous medium and its geometry as well as hydrodynamics. The observed scaling could be universal for other immiscible, two-phase systems in porous media. However, the biofilm being alive leads to changes over time, which is reflected in the temporal evolution of the scaling of the cluster size distribution.

3.2. Time-Resolved Permeability Fields. The method we described (Section 2.3) allowed us to obtain the permeability field of the biofilm-porous medium system from bright-field microscopy images, based on the assumption that the pixel intensity of the biofilm in the gray-scale image corresponds to the local mass per unit volume. This approach,

https://doi.org/10.1021/acs.est.2c08890
Environ. Sci. Technol. 2023, 57, 5666−5677

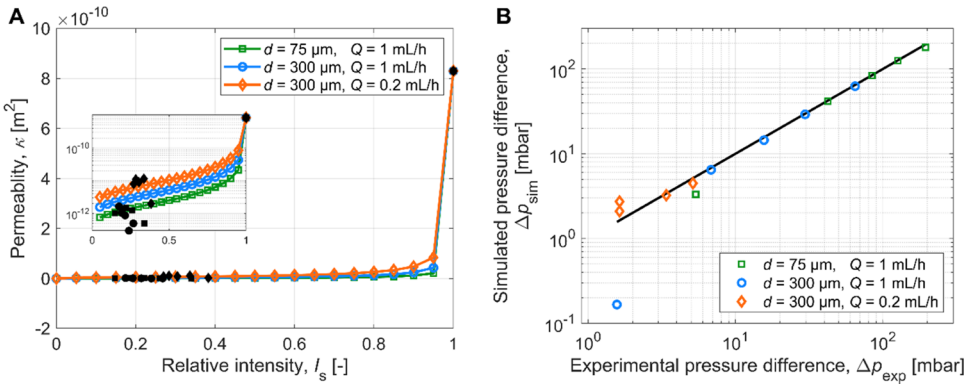

Figure 4. (A) Permeability values obtained from the light transmission model (eq 7), which was fitted to the permeability values κ_{be} and κ_h using a multiobjective calibration approach, as a function of the relative intensity of the bright-field images. The inset shows the same data plotted in a semilog scale. Filled black symbols correspond to the effective permeability values from the biofilm (Section 2.3.1) and open-colored symbols correspond to the fitted permeability model (green square, d = 75 μm, Q = 1 mL/h; blue circle, d = 300 μm, Q = 1 mL/h; orange diamond, d = 300 μm, Q = 0.2 mL/h). The fitted values for α, β, and γ (eq 7) can be found in SI Table S3. (B) Simulated pressure difference between the inlet and the outlet of the porous domain (Δp) obtained from the fluid flow simulations using the permeability fields, as a function of the experimentally measured pressure difference for the same conditions, for different flow rates and pore sizes (legend as in panel (A)). This comparison between the simulated and experimental pressure difference was conducted to validate the calibration in panel (A). The black line denotes $\Delta p_{sim} = \Delta p_{exp}$.

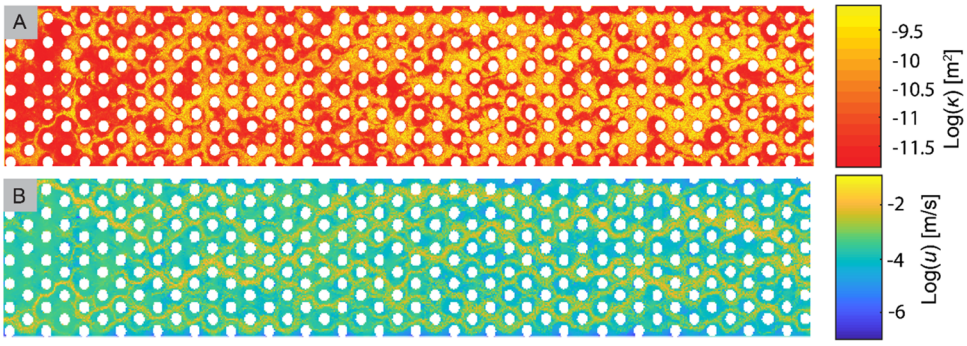

Figure 5. (A) Permeability field of a *B. subtilis* biofilm grown in a microfluidic porous medium with d = 300 μm and Q = 1 mL/h at t = 10 h, corresponding to the experimental images shown in Figure 1A. (B) Spatial distribution of flow velocities computed via a numerical simulation using the permeability field in panel (A).

adapted from methods used for light transmission microtomography, resulted in a model to directly compute a permeability field from images of the system (eq 7). A comparative analysis showed that this model predicted experimentally obtained pressure differences better than three alternative, generic models for computing permeability from images (linear, exponential, and power law) (SI Figure S4).

In each experiment, we performed a multiobjective calibration approach in two stages. First, we fitted the model (eq 7) to the parameters κ_{be}—the permeability that corresponds to the geometric mean of light intensities—and to the parameter κ_h—the maximum permeability that corresponds to a porous medium without biofilm—using the data from the five time points indicated in SI Table S1 (Figure 4A). Second, we simulated the fluid flow velocity and the pressure difference (Δp) with the numerical flow model using the permeability field, then compared the experimentally measured and the simulated pressure difference. We performed this comparison at a time point, t = 15 h, at which the biofilm was well developed under all experimental conditions. These two steps were repeated iteratively until a good agreement, defined as $\Delta p_{exp} - \Delta p_{sim} < 1.5$ mbar, of the experimental and simulated pressure difference at t = 15 h was obtained. Then, to assess the performance of the fitted model, the velocity field and the pressure difference of a further set of four time points from each experiment were simulated using the fitted model and the simulated pressure difference was compared with the experimentally measured one. This comparison revealed good agreement (Figure 4B), with less than 3 mbar difference between the simulated and experimental pressure difference for the majority of time points, demonstrating that the simulation including the permeability field can reproduce the experimentally measured pressure data.

For each experimental condition and time point, we obtained the spatially resolved permeability field from the image intensities using the model in eq 7 (Figure 5A). As expected, the spatial distribution of the permeability has a direct impact on the flow field, resulting in preferential flow paths in regions of high permeability and low-flow regions where permeability is small (Figure 5B). The probability density function of permeability for the biofilm-porous medium system, $p(\kappa)$, calculated from the permeability field reveals how permeability changes over time and varies among experimental conditions. The distribution $p(\kappa)$ exhibits a systematic shift over time, with an increase in low-permeability regions and a decrease in high-permeability regions with time (Figure 6A). This shift arose from the growth of the biofilm as it increased in density and came to occupy an increasing proportion of the pore space, and was observed under all three

https://doi.org/10.1021/acs.est.2c08890
Environ. Sci. Technol. 2023, 57, 5666−5677

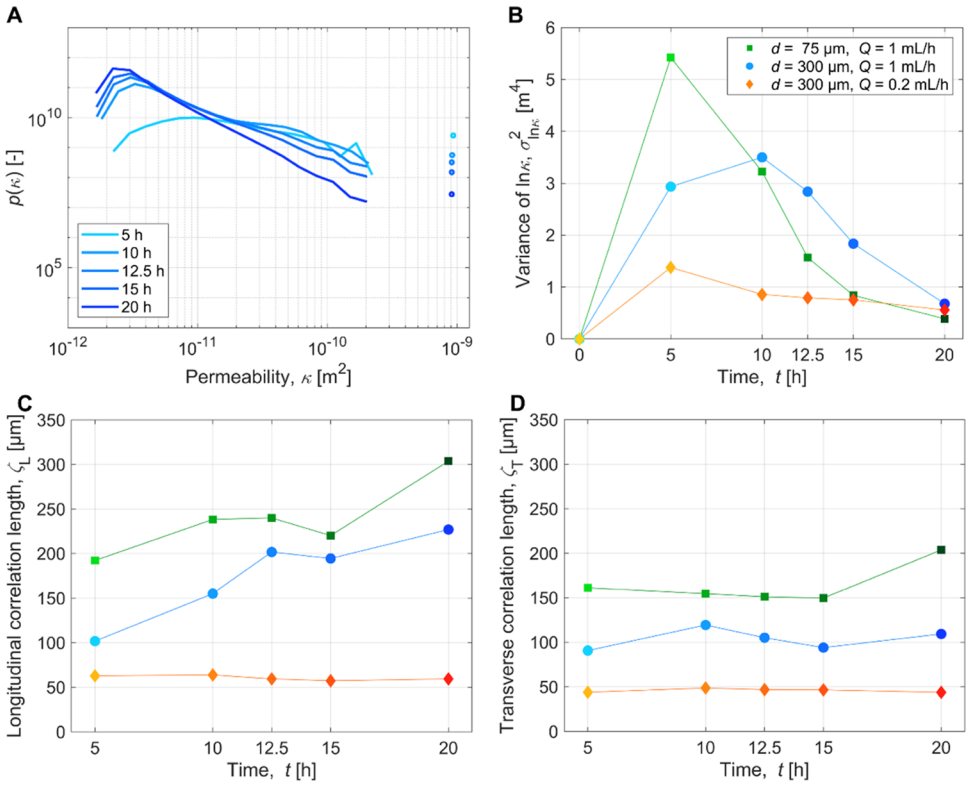

Figure 6. (A) Probability density function of permeability, $p(\kappa)$, for the biofilm-porous medium, for d = 300 μm and Q = 1 mL/h at five time points. Isolated points at $\kappa = 8.3 \times 10^{-10}$ m^2 indicate the probability density of the maximum permeability value, corresponding to a location free of biofilm. The gap in the probability density function is due to the absence of values in this range. The color intensity gradient from lighter to darker indicates the temporal evolution in all panels. (B) Variance of permeability expressed as $\sigma^2_{\ln\kappa}$ as a function of time for the three experimental conditions (greenish squares, d = 75 μm, Q = 1 mL/h; bluish circles, d = 300 μm, Q = 1 mL/h; orangish diamonds, d = 300 μm, Q = 0.2 mL/h). (C, D) Correlation length in the longitudinal direction ζ_L (C) and in the transverse direction ζ_T (D) as a function of time for the same experiments.

experimental conditions (Figure 6A and SI Figure S5). Different from an abiotic system, a biotic system such as a bioclogged porous medium causes these distinct temporally evolving shifts in the distribution of permeability related to the growing biofilm. The decreasing probability of the maximum permeability value ($\kappa_h = 8.3 \times 10^{-10}$ m^2, representing the open pore space) was similarly a result of the biofilm growth. To characterize the probability density function for the permeability of the biofilm $p(\kappa_b)$ several commonly used functions were considered for fitting. We found that the middle section of $p(\kappa_b)$ follows a Gamma distribution more closely than a Normal distribution especially at later time points when the biofilm is well developed (SI Figure S6). The distribution of biofilm permeability has not been previously quantified in a systematic manner for biofilms, and these results could be used to account for the heterogeneity in permeability in simulations of porous media containing biofilms (*e.g.*, to generate equally probable permeability fields using stochastic approaches[70]). This will ultimately help gain a better understanding of the biofilm's impact on velocity distribution and reactive transport.

A larger variance of permeability $\sigma^2_{\ln\kappa}$ indicates greater spatial heterogeneity within the porous medium. We observed an initial increase (t = 5 h for d = 75 μm, Q = 1 mL/h and d = 300 μm, Q = 0.2 mL/h, t = 10 h for d = 300 μm, Q = 1 mL/h) in the heterogeneity of permeability for all three experimental conditions (Figure 6B). The peak in variance was greatest with smaller pore size d = 75 μm and higher flow rate Q, while overall higher variance values were obtained for larger Q at d = 300 μm. After the peak, the heterogeneity in permeability decreased, resulting in a very similar final value independently of d and Q (Figure 6B). This time evolution results from biofilm growth generating heterogeneity, causing the porous medium to initially change from a more homogeneous to a highly heterogeneous permeability field. Once the porous medium is significantly filled with biofilm, it returns to a more homogeneous permeability field due to the similar permeability of the biofilm across the domain. The high peak in variance for d = 75 μm could be explained by the highest number of biofilm clusters in the porous medium (Figure 2C) contributing to permeability heterogeneity. Further, the generally higher variance at higher Q is likely due to higher flow velocities resulting in stronger shear forces, which cause a more heterogeneous degree of biomass densification and therefore a higher permeability variance.

The correlation length, the characteristic distance at which a property remains invariant and typically used as a measure of heterogeneity, was computed from the variogram of permeability. The variogram of permeability values, which is a function of spatial dependence of a random field which commonly follows spherical, power, exponential, or logarithmic models, had the best fit for the exponential model in all experimental conditions. Comparison of the correlation length in the longitudinal and transverse directions with respect to the flow indicates anisotropy, with consistently larger correlation lengths in the longitudinal direction, ζ_L, than in the transverse direction, ζ_T, over all times and across different experiments. More specifically, the ratio ζ_L/ζ_T was between 1.1 and 2.1 (Figure 6C,D; see SI Figure S7 for the omnidirectional

https://doi.org/10.1021/acs.est.2c08890
Environ. Sci. Technol. 2023, 57, 5666−5677

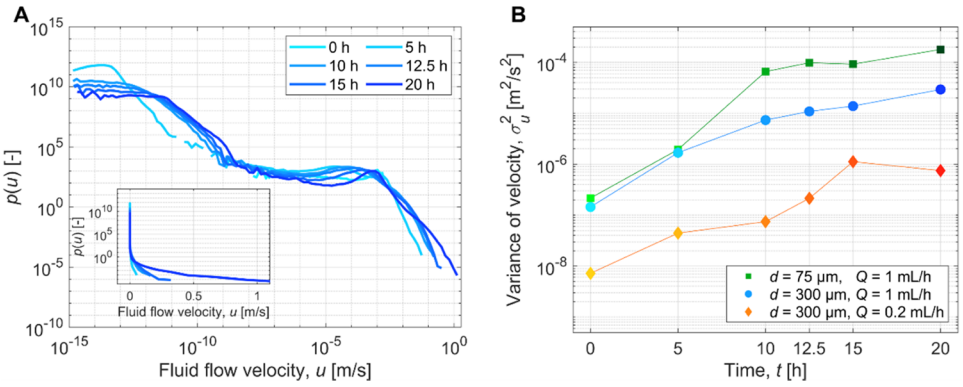

Figure 7. (A) Probability density functions of velocity $p(u)$ for the biofilm−porous medium system with d = 300 μm and Q = 1 mL/h at five time points. The inset shows the same data on a semilogarithmic scale, highlighting the higher velocities. The color gradient indicates the temporal evolution for both panels. (B) Variance of velocity σ_u^2 over time for the three experimental conditions (greenish squares, d = 75 μm, Q = 1 mL/h; bluish circles, d = 300 μm, Q = 1 mL/h; orangish diamonds, d = 300 μm, Q = 0.2 mL/h).

correlation length). The higher correlation in the longitudinal direction, a trend which was stronger for larger Q and smaller d, was imposed by the hydrodynamics of the system, which more strongly reshapes the biofilm in the main flow direction due to stronger shear forces. The anisotropy imposed by the hydrodynamics has also been observed for sedimentary deposits,[71] a larger-scale system. The lower values of $\zeta_L \approx 60$ μm and $\zeta_T \approx 46$ μm for smaller Q at d = 300 μm are explained by the larger number of clusters, which are spatially more homogeneously distributed (Figure 2C) compared to the same pore size at the higher flow rate. This occurs especially at later time points (t > 7.5 h), despite the lower coverage $\sum A$ (Figure 2B), *i.e.*, when the biofilm-porous medium system is highly segregated. Note that for the experiment at d = 75 μm and Q = 1 mL/h (square symbols in Figure 6C,D), a correlation length, ranging 150−300 μm, that is larger than the actual pore size is found, meaning that the biofilm can homogenize the porous medium over a scale that spans several pore sizes.

3.3. Spatio-Temporal Dynamics of Fluid Flow. We computed the probability density function of the flow velocity $p(u)$ from the Eulerian fluid flow velocities obtained by the flow simulations (Figure 5B) for each experiment (Figure 7A and SI Figure S5). The distribution $p(u)$ showed a shift in time with a clear increase in high velocities and a slight decrease in very low velocities. The so-called double structure of the flow field (*i.e.*, the existence of two peaks in $p(u)$) is observed in the presence of biofilm. This was previously observed in single-phase and unsaturated flow in porous media due to structural heterogeneity[72] in the solid phase or due to the presence of an immiscible phase (*e.g.*, air[6]). We further observed that the probability for high velocities follows an exponential trend, $\ln(p(u)) \propto -u$ (inset Figure 7A), which is in agreement with existing literature for unsaturated and bioclogged porous media.[3,6,73] However, in unsaturated porous media, the low velocities in the distribution usually drop off algebraically following a power law ($p(u) \sim u^\theta$ with $\theta < 0$),[6] whereas we instead observed a second peak with a plateau in our biofilm-porous medium system. This can be explained by the permeability heterogeneity within the biofilm, resulting in a more complex system than just a dual-permeability porous medium.[29]

A general increase with time in the variance of velocities σ_u^2 is observed for the three experimental conditions studied (Figure 7B), which confirms results from previous studies of biofilm growth in porous media.[30,74] When comparing the evolution of the variance of the velocities σ_u^2 and the permeability heterogeneity ($\sigma_{\ln\kappa}^2$ and ζ, Figure 6B−D), we observe a peak and decrease in permeability heterogeneity with a continuous increase in σ_u^2. This stands in contrast to the trend commonly observed in porous media, where an increase in the structural heterogeneity[72] or the addition of an immiscible phase (*e.g.*, air[6] or polymers[75]) leading to an increase in permeability heterogeneity, tends to increase σ_u^2. We attribute our finding of a negative correlation between permeability and velocity variance to the permeable nature of the biofilm. The coexistence within the pore space of preferential flow paths and biofilm creates a permeability range that spans three orders of magnitude, but with a declining contribution of high-permeability regions over time to the value of the variance. However, high velocities (up to 1.5 orders of magnitude larger than in the empty porous medium) occur in preferential flow paths and have a large contribution to the variance statistics.

In this work, we have studied the interplay between biofilm formation and some key characteristics of the porous medium, *i.e.*, the pore size and fluid flow velocities. Biofilm formation was studied by characterizing the biofilm cluster size distribution, which revealed that its spectrum slope temporally evolved between −2 and −1. This observation is in agreement with observations from multiphase systems for the slope of −2.[39,67] Further, we believe this temporally evolving scaling is of importance for creating distributions of biofilm clusters to simulate and upscale chemical and reactive transport in bioclogged porous media. Our method to model the resulting flow field by quantifying the permeability field of the biofilm can be used more broadly to shed light on the permeability distribution in biofilms and the temporally resolved evolution of velocities. We found the distribution of biofilm permeability to follow a Gamma distribution better than a Normal distribution for the middle section of the distribution. This permeability distribution can be used to stochastically generate permeability fields of biofilms, likely contributing to improving the predictability of chemical and reactive transport in biofilm-porous medium systems. Furthermore, contrary to findings from unsaturated porous media (with, *e.g.*, air and water), we saw a negative correlation between physical heterogeneity (permeability) and velocity variance.

https://doi.org/10.1021/acs.est.2c08890
Environ. Sci. Technol. 2023, 57, 5666−5677

The relationships between physical heterogeneity and velocity variability are likely to affect solute transport because our results suggest that velocity variance might continue to increase during biofilm growth and cause enhanced chemical dispersion despite a large degree of bioclogging. In general, modeling biofilms as a heterogeneous permeable phase in porous media studies will allow more precise predictions of solute transport and biochemically driven reactions in porous media. As the current study might be considered limited by its two-dimensionality, transferring this approach to a 3D system would permit to further refine the quantitative estimates of heterogeneity in biofilm and hydrodynamic properties obtained here.

■ ASSOCIATED CONTENT

Supporting Information

The Supporting Information is available free of charge at https://pubs.acs.org/doi/10.1021/acs.est.2c08890.

Details on assumption for the derivation of relationship between image intensity and permeability; graphical overview of the methods; probability density functions of the radius of gyration of the experimental replicates; temporal evolution of the spectrum slope; fitting of alternative functions to relate image intensity and permeability; probability density function of permeability and velocity for other experimental conditions; probability density function of biofilm permeability; omnidirectional correlation length; data of image intensity and permeability for fitting of functions; alternative functions; and fitting parameters for eq 7 (PDF)

■ AUTHOR INFORMATION

Corresponding Authors

Eleonora Secchi − *Department of Civil, Environmental and Geomatic Engineering, Institute of Environmental Engineering, ETH Zurich, 8093 Zurich, Switzerland*; Email: esecchi@ethz.ch

Joaquin Jimenez-Martinez − *Department of Civil, Environmental and Geomatic Engineering, Institute of Environmental Engineering, ETH Zurich, 8093 Zurich, Switzerland; Department Water Resources and Drinking Water, Eawag, Swiss Federal Institute of Aquatic Science and Technology, 8600 Dübendorf, Switzerland;* orcid.org/0000-0002-2063-6490; Email: joaquin.jimenez@eawag.ch

Authors

Dorothee L. Kurz − *Department of Civil, Environmental and Geomatic Engineering, Institute of Environmental Engineering, ETH Zurich, 8093 Zurich, Switzerland; Department Water Resources and Drinking Water, Eawag, Swiss Federal Institute of Aquatic Science and Technology, 8600 Dübendorf, Switzerland;* orcid.org/0000-0002-3428-342X

Roman Stocker − *Department of Civil, Environmental and Geomatic Engineering, Institute of Environmental Engineering, ETH Zurich, 8093 Zurich, Switzerland*

Complete contact information is available at: https://pubs.acs.org/10.1021/acs.est.2c08890

Notes

The authors declare no competing financial interest.

■ ACKNOWLEDGMENTS

The authors acknowledge support from SNSF PRIMA grant 179834 (to E.S.), discretionary funding from ETH (to R.S.), an ETH Zurich Research Grant (to R.S. and J.J.M.), and discretionary funding from Eawag (to J.J.M.).

■ REFERENCES

(1) Flemming, H. C.; Wuertz, S. Bacteria and Archaea on Earth and Their Abundance in Biofilms. *Nat. Rev. Microbiol.* **2019**, *17*, 247−260.

(2) Cunningham, A. B.; Characklls, W. G.; Abedeen, F.; Crawford, D. Influence of Biofilm Accumulation on Porous Media Hydrodynamics. *Environ. Sci. Technol.* **1991**, *25*, 1305−1311.

(3) Carrel, M.; Morales, V. L.; Dentz, M.; Derlon, N.; Morgenroth, E.; Holzner, M. Pore-Scale Hydrodynamics in a Progressively Bioclogged Three-Dimensional Porous Medium: 3-D Particle Tracking Experiments and Stochastic Transport Modeling. *Water Resour. Res.* **2018**, *54*, 2183−2198.

(4) Durham, W. M.; Tranzer, O.; Leombruni, A.; Stocker, R. Division by Fluid Incision: Biofilm Patch Development in Porous Media. *Phys. Fluids* **2012**, *24*, No. 091107.

(5) Stewart, T. L.; Fogler, S. H. Pore-Scale Investigation of Biomass Plug Development and Propagation in Porous Media. *Biotechnol. Bioeng.* **2002**, *77*, 577−588.

(6) Velásquez-Parra, A.; Aquino, T.; Willmann, M.; Méheust, Y.; Le Borgne, T.; Jiménez-Martínez, J. Sharp Transition to Strongly Anomalous Transport in Unsaturated Porous Media. *Gephys. Res. Lett.* **2022**, *49*. DOI: 10.1029/2021GL096280.

(7) Bottero, S.; Storck, T.; Heimovaara, T. J.; van Loosdrecht, M. C. M.; Enzien, M. V.; Picioreanu, C. Biofilm Development and the Dynamics of Preferential Flow Paths in Porous Media. *Biofouling* **2013**, *29*, 1069−1086.

(8) Sharp, R. R.; Stoodley, P.; Adgie, M.; Gerlach, R.; Cunningham, A. Visualization and Characterization of Dynamic Patterns of Flow, Growth and Activity of Biofilms Growing in Porous Media. *Water Sci. Technol.* **2005**, *52*, 85−90.

(9) Pintelon, T. R. R.; Picioreanu, C.; van Loosdrecht, M. C. M.; Johns, M. L. The Effect of Biofilm Permeability on Bio-Clogging of Porous Media. *Biotechnol. Bioeng.* **2012**, *109*, 1031−1042.

(10) Cunningham, A. B.; Sharp, R. R.; Hiebert, R.; James, G. Subsurface Biofilm Barriers for the Containment and Remediation of Contaminated Groundwater. *Biorem. J.* **2003**, *7*, 151−164.

(11) Baveye, P.; Vandevivere, P.; Hoyle, B. L.; DeLeo, P. C.; Sanchez De Lozada, D. Environmental Impact and Mechanisms of the Biological Clogging of Saturated Soils and Aquifer Materials. *Crit. Rev. Environ. Sci. Technol.* **1998**, *28*, 123−191.

(12) Mitchell, J. K.; Santamarina, J. C. Biological Considerations in Geotechnical Engineering. *J. Geotech. Geoenviron. Eng.* **2005**, *131*, 1222−1233.

(13) Flemming, H. C.; Wingender, J. The Biofilm Matrix. *Nat. Rev. Microbiol.* **2010**, *8*, 623−633.

(14) Wilking, J. N.; Zaburdaev, V.; De Volder, M.; Losick, R.; Brenner, M. P.; Weitz, D. A. Liquid Transport Facilitated by Channels in *Bacillus Subtilis* Biofilms. *Proc. Natl. Acad. Sci. U.S.A.* **2013**, *110*, 848−852.

(15) Rooney, L. M.; Amos, W. B.; Hoskisson, P. A.; McConnell, G. Intra-Colony Channels in E. Coli Function as a Nutrient Uptake System. *ISME J.* **2020**, *14*, 2461−2473.

(16) Bottura, B.; Rooney, L. M.; Hoskisson, P. A.; McConnell, G. Intra-Colony Channel Morphology in Escherichia Coli Biofilms Is Governed by Nutrient Availability and Substrate Stiffness. *bioRxiv* **2021**, DOI: 10.1101/2021.12.17.473116.

(17) Quan, K.; Hou, J.; Zhang, Z.; Ren, Y.; Peterson, B. W.; Flemming, H. C.; Mayer, C.; Busscher, H. J.; van der Mei, H. C. Water in Bacterial Biofilms: Pores and Channels, Storage and Transport Functions. *Crit. Rev. Microbiol.* **2022**, *48*, 283−302.

(18) Mandelbrot, B. B.; Wheeler, J. A. The Fractal Geometry of Nature. *Am. J. Phys.* **1983**, *51*, 286−287.

(19) Hermanowicz, S. W.; Schindler, U.; Wilderer, P. Anisotropic Morphology and Fractal Dimension of Biofilms. *Water Res.* **1996**, *30*, 753−755.
(20) Picioreanu, C.; Van Loosdrecht, M. C. M.; Heijnen, J. J. Mathematical Modeling of Biofilm Structure with a Hybrid Differential- Discrete Cellular Automaton Approach. *Biotechnol. Bioeng.* **1998**, *58*, 101−116.
(21) Kim, J. W.; Choi, H.; Pachepsky, Y. A. Biofilm Morphology as Related to the Porous Media Clogging. *Water Res.* **2010**, *44*, 1193−1201.
(22) Zahid, W.; Ganczarczyk, J. A Technique for a Characterization of RBC Biofilm Surface. *Water Res.* **1994**, *28*, 2229−2231.
(23) Moreau, A. L. D.; Lorite, G. S.; Rodrigues, C. M.; Souza, A. A.; Cotta, M. A. Fractal Analysis of Xylella Fastidiosa Biofilm Formation. *J. Appl. Phys.* **2009**, *106*, No. 024702.
(24) Yang, X.; Beyenal, H.; Harkin, G.; Lewandowski, Z. Quantifying Biofilm Structure Using Image Analysis. *J. Microbiol. Methods* **2000**, *39*, 109−119.
(25) Lewandowski, Z.; Webb, D.; Hamilton, M.; Harkin, G. Quantifying Biofilm Structure. *Water Sci. Technol.* **1999**, *39*, 71−76.
(26) Carrel, M.; Morales, V.; Beltran, M.; Derlon, N.; Kaufmann, R.; Morgenroth, E.; Holzner, M. Biofilms in 3D Porous Media: Delineating the Influence of the Pore Network Geometry, Flow and Mass Transfer on Biofilm Development. *Water Res.* **2018**, *134*, 280−291.
(27) Aufrecht, J. A.; Fowlkes, J. D.; Bible, A. N.; Morrell-Falvey, J.; Doktycz, M. J.; Retterer, S. T. Pore-Scale Hydrodynamics Influence the Spatial Evolution of Bacterial Biofilms in a Microfluidic Porous Network. *PLoS One* **2019**, *14*, No. e0218316.
(28) Deng, W.; Cardenas, M. B.; Kirk, M. F.; Altman, S. J.; Bennett, P. C. Effect of Permeable Biofilm on Micro-and Macro-Scale Flow and Transport in Bioclogged Pores. *Environ. Sci. Technol.* **2013**, *47*, 11092−11098.
(29) Karimifard, S.; Li, X.; Elowsky, C.; Li, Y. Modeling the Impact of Evolving Biofilms on Flow in Porous Media inside a Microfluidic Channel. *Water Res.* **2021**, *188*, No. 116536.
(30) Perez, L. J.; Parashar, R.; Plymale, A.; Scheibe, T. D. Contributions of Biofilm-Induced Flow Heterogeneities to Solute Retention and Anomalous Transport Features in Porous Media. *Water Res.* **2022**, *209*, No. 117896.
(31) Peszynska, M.; Trykozko, A.; Iltis, G.; Schlueter, S.; Wildenschild, D. Biofilm Growth in Porous Media: Experiments, Computational Modeling at the Porescale, and Upscaling. *Adv. Water Resour.* **2016**, *95*, 288−301.
(32) Zhang, T. C.; Bishop, P. L. Density, Porosity, and Pore Structure of Biofilms. *Water Res.* **1994**, *28*, 2267−2277.
(33) Jung, H.; Meile, C. Pore-Scale Numerical Investigation of Evolving Porosity and Permeability Driven by Biofilm Growth. *Transp. Porous Media* **2021**, *139*, 203−221.
(34) Hassannayebi, N.; Jammernegg, B.; Schritter, J.; Arnold, P.; Enzmann, F.; Kersten, M.; Loibner, A. P.; Fernø, M.; Ott, H. Relationship Between Microbial Growth and Hydraulic Properties at the Sub-Pore Scale. *Transp. Porous Media* **2021**, *139*, 579−593.
(35) de Anna, P.; Jimenez-Martinez, J.; Tabuteau, H.; Turuban, R.; Le Borgne, T.; Derrien, M.; Méheust, Y. Mixing and Reaction Kinetics in Porous Media: An Experimental Pore Scale Quantification. *Environ. Sci. Technol.* **2014**, *48*, 508−516.
(36) Markale, I.; Cimmarusti, G. M.; Britton, M. M.; Jiménez-Martínez, J. Phase Saturation Control on Mixing-Driven Reactions in 3D Porous Media. *Environ. Sci. Technol.* **2021**, *55*, 8742−8752.
(37) Kurz, D. L.; Secchi, E.; Stocker, R.; Jimenez-Martinez, J. A Microfluidic Platform to Study Bioclogging in Porous Media. *J. Vis. Exp.* **2022**, *188*, No. e64689.
(38) Schneider, C. A.; Rasband, W. S.; Eliceiri, K. W. NIH Image to ImageJ: 25 Years of Image Analysis. *Nat. Methods* **2012**, *9*, 671−675.
(39) Jiménez-Martínez, J.; Le Borgne, T.; Tabuteau, H.; Méheust, Y. Impact of Saturation on Dispersion and Mixing in Porous Media: Photobleaching Pulse Injection Experiments and Shear-Enhanced Mixing Model. *Water Resour. Res.* **2017**, *53*, 1457−1472.
(40) Leggett, S. E.; Neronha, Z. J.; Bhaskar, D.; Sim, J. Y.; Perdikari, T. M.; Wong, I. Y. Motility-Limited Aggregation of Mammary Epithelial Cells into Fractal-like Clusters. *Proc. Natl. Acad. Sci. U.S.A.* **2019**, *116*, 17298−17306.
(41) Durlofsky, L.; Brady, J. F. Analysis of the Brinkman Equation as a Model for Flow in Porous Media. *Phys. Fluids* **1987**, *30*, 3329−3341.
(42) Ferrari, A.; Jimenez-Martinez, J.; Le Borgne, T.; Méheust, Y.; Lunati, I. Challenges in Modeling Unstable Two-Phase Flow Experiments in Porous Micromodels. *Water Resour. Res.* **2015**, *51*, 1381−1400.
(43) Soulaine, C.; Maes, J.; Roman, S. Computational Microfluidics for Geosciences. *Front. Water* **2021**, *3*, No. 643714.
(44) Lewandowski, Z. Notes on Biofilm Porosity. *Water Res.* **2000**, *34*, 2620−2624.
(45) Matheron, G. *Elements Pour une Théorie des Milieux Poreux*, Paris, 1967.
(46) Masihi, M.; Gago, P. A.; King, P. R. Estimation of the Effective Permeability of Heterogeneous Porous Media by Using Percolation Concepts. *Transp. Porous Media* **2016**, *114*, 169−199.
(47) Wu, M.; Cheng, Z.; Wu, J.; Wu, J. Precise Simulation of Long-Term DNAPL Migration in Heterogeneous Porous Media Based on Light Transmission Micro-Tomography. *J. Environ. Chem. Eng.* **2017**, *5*, 725−734.
(48) Wu, M.; Cheng, Z.; Wu, J.; Wu, J.; Hu, X. Effects of Inner Heterogeneity on Long-Term DNAPL Migration in Porous Media. *Environ. Earth Sci.* **2017**, *76*, No. 791.
(49) Brooks, R. H.; Corey, A. T. *Hydraulic Properties of Porous Media*; Brooks, R. H.; Corey, A. T., Eds.; Hydrology papers/Colorado State University no. 3; Colorado State University: Fort Collins, Col, 1964.
(50) Hommel, J.; Coltman, E.; Class, H. Porosity−Permeability Relations for Evolving Pore Space: A Review with a Focus on (Bio-)Geochemically Altered Porous Media. *Transp. Porous Media* **2018**, *124*, 589−629.
(51) Wackernagel, H. *Multivariate Geostatistics an Introduction with Applications*, 3rd, compled.; Springer: Berlin, 2003.
(52) Zinn, B.; Harvey, C. F. When Good Statistical Models of Aquifer Heterogeneity Go Bad: A Comparison of Flow, Dispersion, and Mass Transfer in Connected and Multivariate Gaussian Hydraulic Conductivity Fields. *Water Resour. Res.* **2003**, *39*, No. 1051.
(53) Salamon, P.; Fernàndez-Garcia, D.; Gómez-Hernández, J. J. Modeling Tracer Transport at the MADE Site: The Importance of Heterogeneity. *Water Resour. Res.* **2007**, *43*, No. W08404.
(54) Thomen, P.; Valentin, J. D. P.; Bitbol, A. F.; Henry, N. Spatiotemporal Pattern Formation in: E. Coli Biofilms Explained by a Simple Physical Energy Balance. *Soft Matter* **2020**, *16*, 494−504.
(55) Cates, M. E.; Marenduzzo, D.; Pagonabarraga, I.; Tailleur, J. Arrested Phase Separation in Reproducing Bacteria Creates a Generic Route to Pattern Formation. *Proc. Natl. Acad. Sci. U.S.A.* **2010**, *107*, 11715−11720.
(56) Hödl, I.; Mari, L.; Bertuzzo, E.; Suweis, S.; Besemer, K.; Rinaldo, A.; Battin, T. J. Biophysical Controls on Cluster Dynamics and Architectural Differentiation of Microbial Biofilms in Contrasting Flow Environments. *Environ. Microbiol.* **2014**, *16*, 802−812.
(57) Depetris, A.; Peter, H.; Bordoloi, A. D.; Bernard, H.; Niayifar, A.; Kühl, M.; de Anna, P.; Battin, T. J. Morphogenesis and Oxygen Dynamics in Phototrophic Biofilms Growing across a Gradient of Hydraulic Conditions. *iScience* **2021**, *24*, No. 102067.
(58) Zhang, Q.; Li, J.; Nijjer, J.; Lu, H.; Kothari, M.; Alert, R.; Cohen, T.; Yan, J. Morphogenesis and Cell Ordering in Confined Bacterial Biofilms. *Proc. Natl. Acad. Sci. U.S.A.* **2021**, *118*, No. e2107107118.
(59) Li, J.; Kothari, M.; Chockalingam, S.; Henzel, T.; Zhang, Q.; Li, X.; Yan, J.; Cohen, T. Nonlinear Inclusion Theory with Application to the Growth and Morphogenesis of a Confined Body. *J. Mech. Phys. Solids* **2022**, *159*, No. 104709.
(60) Kurz, D. L.; Secchi, E.; Carrillo, F. J.; Bourg, I. C.; Stocker, R.; Jimenez-Martine, J. Competition between Growth and Shear Stress

https://doi.org/10.1021/acs.est.2c08890
Environ. Sci. Technol. 2023, 57, 5666−5677

Drives Intermittency in Preferential Flow Paths in Porous Medium Biofilms. *Proc. Natl. Acad. Sci. U.S.A.* **2022**, *119*, No. e2122202119.
(61) Kolb, M.; Herrmanne, H. J. The Sol-Gel Transition Modelled by Irreversible Aggregation of Clusters. *J. Phys. A: Math. Gen.* **1985**, *18*, L435−L441.
(62) Berkowitz, B.; Balberg, I. Percolation Theory and Its Application to Groundwater Hydrology. *Water Resour. Res.* **1993**, *29*, 775−794.
(63) Lazzari, S.; Nicoud, L.; Jaquet, B.; Lattuada, M.; Morbidelli, M. Fractal-like Structures in Colloid Science. *Adv. Colloid Interface Sci.* **2016**, *235*, 1−13.
(64) Maggi, F. Experimental Evidence of How the Fractal Structure Controls the Hydrodynamic Resistance on Granular Aggregates Moving through Water. *J. Hydrol.* **2015**, *528*, 694−702.
(65) Adrover, A.; Giona, M. Hydrodynamic Properties of Fractals: Application of the Lattice Boltzmann Equation to Transverse Flow Past an Array of Fractal Objects. *Int. J. Multiphase Flow* **1997**, *23*, 25−35.
(66) Stauffer, D.; Aharony, A. *Introduction to Percolation Theory*, 2nd ed.; Taylor & Francis: Boca Raton, FL, 2014.
(67) Tallakstad, K. T.; Løvoll, G.; Knudsen, H. A.; Ramstad, T.; Flekkøy, E. G.; Måløy, K. J. Steady-State, Simultaneous Two-Phase Flow in Porous Media: An Experimental Study. *Phys. Rev. E* **2009**, *80*, No. 036308.
(68) Baldy, S.; Bourguel, M. Bubbles between the Wave Trough and Wave Crest Levels. *J. Geophys. Res. Ocean.* **1987**, *92*, 2919−2929.
(69) Ramstad, T.; Hansen, A. Cluster Evolution in Steady-State Two-Phase Flow in Porous Media. *Phys. Rev. E* **2006**, *73*, No. 026306.
(70) Räss, L.; Kolyukhin, D.; Minakov, A. Efficient Parallel Random Field Generator for Large 3-D Geophysical Problems. *Comput. Geosci.* **2019**, *131*, 158−169.
(71) Rubin, Y. *Applied Stochastic Hydrogeology; Oxford Scholarship Online*; Oxford University Press: Oxford; 2003.
(72) Holzner, M.; Morales, V. L.; Willmann, M.; Dentz, M. Intermittent Lagrangian Velocities and Accelerations in Three-Dimensional Porous Medium Flow. *Phys. Rev. E* **2015**, *92*, No. 013015.
(73) Datta, S. S.; Chiang, H.; Ramakrishnan, T. S.; Weitz, D. A. Spatial Fluctuations of Fluid Velocities in Flow through a Three-Dimensional Porous Medium. *Phys. Rev. Lett.* **2013**, *111*, No. 064501.
(74) Seymour, J. D.; Gage, J. P.; Codd, S. L.; Gerlach, R. Anomalous Fluid Transport in Porous Media Induced by Biofilm Growth. *Phys. Rev. Lett.* **2004**, *93*, No. 198103.
(75) Parsa, S.; Zareei, A.; Santanach-Carreras, E.; Morris, E. J.; Amir, A.; Xiao, L.; Weitz, D. A. Unexpected Scaling of Interstitial Velocities with Permeability Due to Polymer Retention in Porous Media. *Phys. Rev. Fluids* **2021**, *6*, No. L082302.

https://doi.org/10.1021/acs.est.2c08890
Environ. Sci. Technol. 2023, 57, 5666−5677